Reconfigurable Metasurface Aperture for Integrated Compressive Electromagnetic Sensing and Imaging

Mengran Zhao[1], Mohsen Khalily[2], Insang Yoo[3], Trung Q. Duong[4], Simon Cotton[1], and Okan Yurduseven[1]
[1]Centre for Wireless Innovation, Queen's University Belfast, BT3 9DT Belfast, U.K.
[2]Institute for Communication Systems, University of Surrey, GU2 7XH Guildford, U.K.
[3]Department of Electrical and Electronic Engineering, Yonsei University, 50 Yonsei-ro Seodaemun-gu Seoul, Korea
[4]Faculty of Engineering and Applied Science, Memorial University of Newfoundland, A1B 3X7 St. John's, Canada

***Abstract*—In this paper, a reconfigurable metasurface aperture (RMA) is proposed for integrated compressive electromagnetic sensing and imaging (ISAI) applications. The proposed RMA consists of randomly distributed switchable meta-atoms with two orthogonal orientations to enable dual-polarized radiation. The meta-atoms are loaded with PIN diodes, and by reconfiguring their operating states, the meta-atoms are selectively deactivated or activated. This dynamic mechanism is used to reconfigure the aperture state of metasurface and generate spatially low-correlated radiation patterns. These patterns serve as measurement modes for ISAI implementation. The performance of RMA is characterized using the reflection coefficient (S_{11}) to assess the antenna behavior, and the correlation coefficient (CC) and the singular value (SV) spectrum to evaluate the spatial orthogonality of its measurement modes. An RMA-based ISAI study is conducted to validate the proposed design, in which the incident angles of far-field sources are accurately estimated and both the image and orientation of a target are successfully retrieved, confirming the effectiveness of the approach.**

***Index Terms*—Computational imaging, DoA estimation, integrated sensing and imaging, reconfigurable metasurface aperture.**

I. Introduction

With the rapid development of the Internet of Things (IoT), the capability to accurately localize and identify targets has become increasingly critical for advanced sensing applications, such as autonomous driving [1], healthcare monitoring [2], and security screening [3], to name a few.

Traditional localization techniques are typically classified into time-of-arrival (ToA) [4] and direction-of-arrival (DoA) [5] methods. ToA approaches require ultra-wideband (UWB) hardware to accurately measure the propagation delay between transmitted and received signals [4]. In contrast, DoA techniques rely on multiple synchronized sensors and computationally intensive beamforming algorithms [6]. These requirements lead to increased hardware complexity, power consumption, and system cost, making both approaches less suitable for low-power, resource-constrained IoT applications.

Similarly, microwave imaging, widely used for target identification, also faces significant limitations in IoT scenarios. Conventional methods, such as synthetic aperture radar (SAR) [7] and phased array radar (PAR) [8], primarily depend on raster-scanning strategies to achieve high-resolution image reconstruction. These approaches, although effective, suffer from either slow mechanical movement or considerable hardware overhead, which limits their real-time capability and increases system complexity and power consumption.

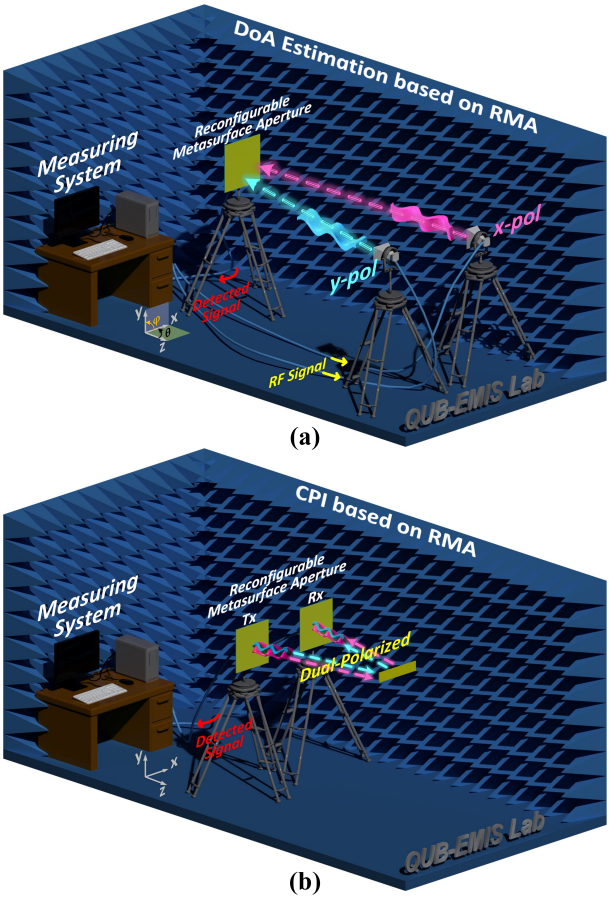

Fig. 1. Configuration of the RMA-based ISAI. (a) DoA estimation based on the RMA; (b) CI based on the RMA.

To address these challenges, as shown in Fig. 1, the concept of compressive sensing (CS) has emerged as an effective and promising paradigm. Within the framework of computational imaging (CI) [9], [10], CS enables scene reconstruction from a significantly reduced number of measurements. These measurements encode scene information into a set of compressed signals, thereby eliminating the need for conventional raster-scan approaches [11], [12]. Furthermore, when the projection

of a far-field source is treated as an imaged target, the incident angles can be efficiently estimated using the same CI architecture [13], [14], [15]. Consequently, both identification and localization can be realized with fewer radio frequency (RF) components, reduced energy consumption, and simplified system architectures—characteristics that align well with the demands of IoT applications.

Among the most promising technologies enabling CS-driven imaging and DoA estimation are metasurface-based wave-chaotic antennas [16], [17], [18], [19]. These metasurfaces are designed to generate spatially orthogonal radiation patterns through either frequency diversity [20], [21], [22] or reconfigurable control [23], [24], [25], [26]. Frequency-diverse metasurfaces produce varying fields by sweeping across frequencies, whereas reconfigurable metasurfaces employ tunable components, such as PIN diodes, to alter their response across a narrow frequency band (and even at a single frequency), thereby reducing the required system bandwidth and simplifying the design of broadband RF chains. However, most existing metasurface designs treat DoA estimation and imaging as separate functions requiring multiple hardware sources, with limited progress toward integrating both within a single platform. In addition, current implementations are generally limited to single-polarization operation, lacking the ability to distinguish the polarization state of far-field sources or to extract the geometric features of the imaged target—capabilities that can be achieved through computational polarimetric imaging techniques [27], [28], [29], [30], [31].

To address the aforementioned issues, in this paper, we propose a reconfigurable metasurface aperture (RMA) capable of radiating dual-polarized, spatially low-correlated field patterns. By randomly switching the operating states (*on/off*) of the PIN diodes loaded onto the RMA, different radiating elements are selectively deactivated or activated, thereby altering the aperture distribution (or *mask*) of the RMA, producing diverse radiation patterns. These patterns function as *measurement modes* for implementing the proposed integrated compressive electromagnetic sensing and imaging (ISAI) technique (i.e., DoA estimation and CI) [32] using a unified hardware platform, as illustrated in Fig. 1.

The rest of this paper is organized as follows. Section II briefly introduces the ISAI process based on the RMA, laying a foundation for the subsequent sections. Section III details the design of the RMA and evaluates its performance. In Section IV, ISAI experiments are performed using the proposed RMA. Finally, Section V concludes the paper.

II. Process of the RMA-based ISAI

The RMA-based ISAI, as depicted in Fig. 1, consists of two parts: RMA-based DoA estimation and RMA-based CI. For RMA-based DoA estimation, a single RMA is employed as a receiver (Rx), whereas for RMA-based CI, two distinct RMAs are used as a transmitter (Tx) and an Rx, respectively. Under this configuration and in accordance with the first Born approximation [33], the back-scattered data, $g^{s_j}(f)$, for DoA estimation and CI can be respectively expressed as follows:

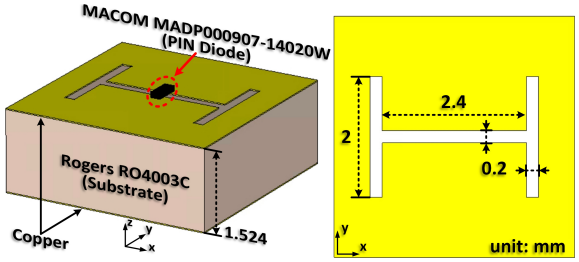

Fig. 2. Schematic diagram of the switchable meta-atom.

$$g_{DoA}^{s_r^j}(f) = \int_{\boldsymbol{r}} \mathbf{E}_{\mathrm{R}}^{s_r^j}(\boldsymbol{r}, f) \cdot \boldsymbol{p}(\boldsymbol{r}) d\boldsymbol{r} \tag{1}$$

$$g_{CI}^{s_t^i, s_r^j}(f) = \int_{\boldsymbol{r}} \mathbf{E}_{\mathrm{T}}^{s_t^i}(\boldsymbol{r}, f) \cdot \mathbf{E}_{\mathrm{R}}^{s_r^j}(\boldsymbol{r}, f) \cdot \boldsymbol{\chi}(\boldsymbol{r}) d\boldsymbol{r} \tag{2}$$

where $\mathbf{E}_{\mathrm{T}}$ and $\mathbf{E}_{\mathrm{R}}$ denote the radiated field patterns of the Tx and Rx, respectively. s_t^i and s_r^j represent the i-th mask of the Tx and the j-th mask of the Rx, respectively. $\boldsymbol{p}$ refers to the projection of the fields radiated by the far-field sources on to a plane in front of the RMA whereas $\boldsymbol{\chi}$ denotes the susceptibility tensor of the imaged scene [29]. $\boldsymbol{r}$ denotes the position vector of an imaged pixel [34], and f represents the operating frequency. Here, the bold font indicates the vector-matrix notation.

The above two processes can be simply denoted as:

$$\boldsymbol{g} = \mathbf{H} \cdot \boldsymbol{\sigma} \tag{3}$$

where $\mathbf{H}$ represents the *sensing matrix* constructed from a set of measurement modes [32], and $\boldsymbol{\sigma}$ denotes the estimated objective (i.e., $\boldsymbol{p}$ or $\boldsymbol{\chi}$).

Consequently, the projection pattern (or imaged scene) can be reconstructed using computational algorithms, such as the least-squares algorithm [35]:

$$\boldsymbol{\sigma}_{est} = \arg\min_{\boldsymbol{\sigma}} \left\| \boldsymbol{g} - \mathbf{H}\boldsymbol{\sigma} \right\|_2^2 \tag{4}$$

III. Design of the RMA

According to the analysis in Section II, the RMA should be capable of radiating diverse field patterns. Therefore, it is essential to rapidly reconfigure the mask across the RMA. To this end, a single-polarized switchable meta-atom is designed as the radiating element, which can be deactivated or activated by toggling the operating states (*on/off*) of the PIN diodes loaded on it. Subsequently, by randomly arranging the meta-atoms with two orthogonal orientations over the aperture, an RMA capable of radiating dual-polarized, low-correlated field patterns is realized.

A. Switchable Meta-Atom

As shown in Fig. 2, an "I-shaped" meta-atom is etched on the top layer of the substrate to function as the radiating element, while the backside of the substrate is copper-clad

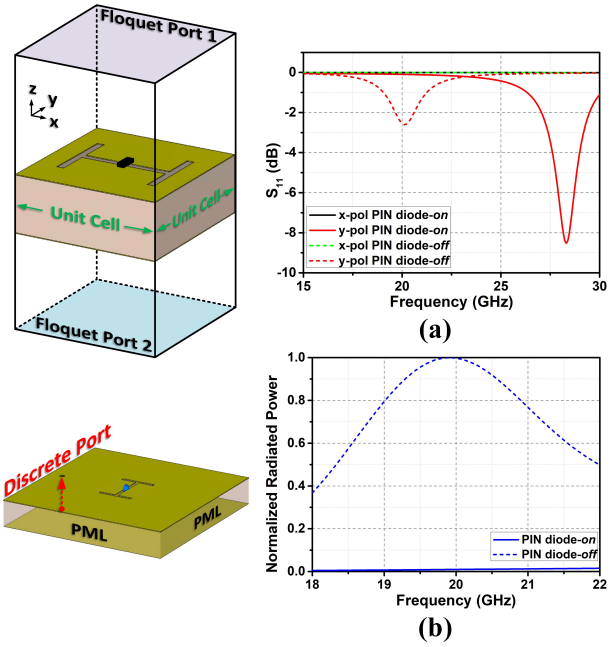

Fig. 3. Performance analysis of the switchable meta-atom based on (a) the Floquet port model and (b) the radiating model.

to form the ground plane. The meta-atom has a side length of 4 mm, and its structural parameters are detailed in Fig. 2. The substrate is Rogers RO4003C (ε_r = 3.35, $tan\delta$ = 0.0027) with a thickness of 1.524 mm and the PIN diode is MACOM MADP000907-14020W. The PIN diode can be modeled as a resistor-inductor-capacitor (RLC) series circuit with parameters R = 5 Ω, L = 0.1 nH for *on* state (+1.4 V) and R = 10 kΩ, L = 0.1 nH, C = 0.025 pF for *off* state (-10 V) [19], [30].

The performance of the "I-shaped" meta-atom is evaluated in CST Microwave Studio using two approaches: the Floquet port model and the radiating model, as shown in Fig. 3(a) and 3(b). From Fig. 3(a), it can be observed that the "I-shaped" meta-atom only works under y-polarization and is activated at 20 GHz when the PIN diode is *off*. Conversely, when the PIN diode is in *on* state, the meta-atom is deactivated at 20 GHz, demonstrating a switch-like behavior. The normalized radiated power obtained from the radiating model, as shown in Fig. 3(b), further confirms this characteristic.

B. RMA and Its Performance

Considering that the switchable meta-atom radiates only single-polarized field patterns, and dual-polarized radiation is required for the RMA, it is therefore necessary to rotate a portion of the meta-atoms by 90° to achieve this functionality. Thus, as shown in Fig. 4, the RMA is realized by randomly distributing 492 switchable meta-atoms across the aperture, with half of them rotated by 90°. The overall dimensions of the RMA are 6.67λ × 6.67λ (100 mm × 100 mm), where λ denotes the free-space wavelength at 20 GHz.

The performance of the proposed RMA is evaluated as shown in Fig. 5. First of all, the reflection coefficient (i.e., S_{11}) of the RMA is assessed to characterize its antenna behavior.

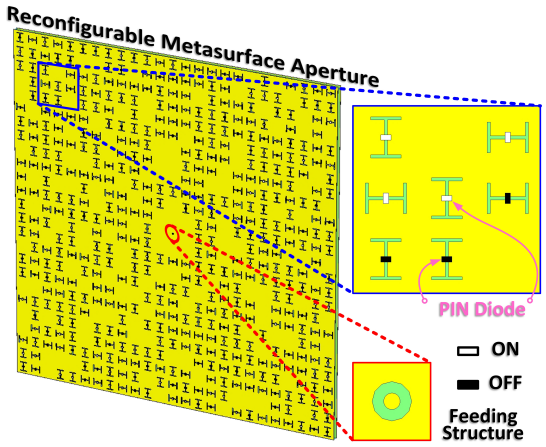

Fig. 4. Schematic of the RMA with half meta-atoms rotated by 90°.

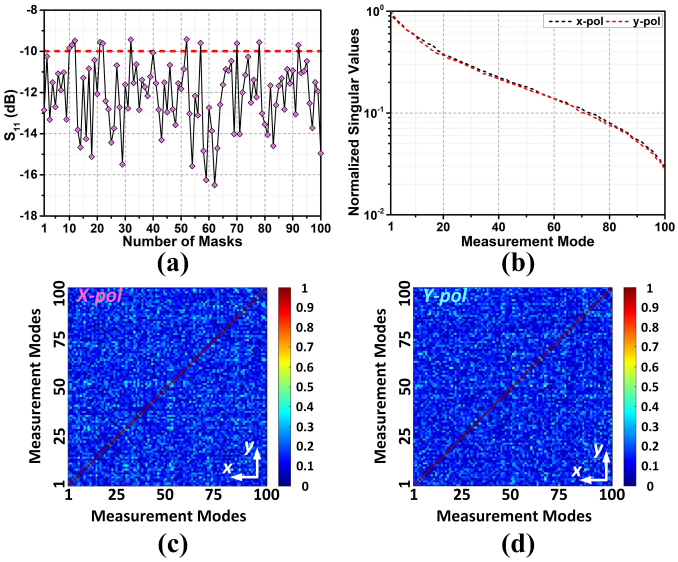

Fig. 5. (a) Reflection coefficients (S_{11}) of the RMA under different masks; (b) SV curves of both the x- and y-polarized measurement modes; CC values of the (c) x-polarized and (d) y-polarized measurement modes.

From Fig. 5(a), the S_{11} values under most mask configurations remain below -10 dB, indicating a good impedance matching of the RMA. Then, considering that the RMA is specifically designed for ISAI applications, it is essential to evaluate the spatial orthogonality of the measurement modes ($\mathbf{H} = \mathbf{E}_{\mathrm{T}} \cdot \mathbf{E}_{\mathrm{R}}$). Common metrics for this assessment include the correlation coefficient (CC) [35] and singular value (SV) [36]. Generally, better performance is indicated by lower CC values and a flatter SV spectrum [37]. Here, as an example and without loss of generality, 100 measurement modes are selected to verify the performance. As depicted in Fig. 5(b), the normalized SVs of the measurement modes under dual-polarization states are above 10^{-2} and form two relatively flat curves, indicating high spatial orthogonality [38]. Furthermore, as illustrated in Fig. 5(c) and 5(d), the CC values for both x- and y-polarized measurement modes are smaller than 0.26, confirming their low-correlation characteristics [39].

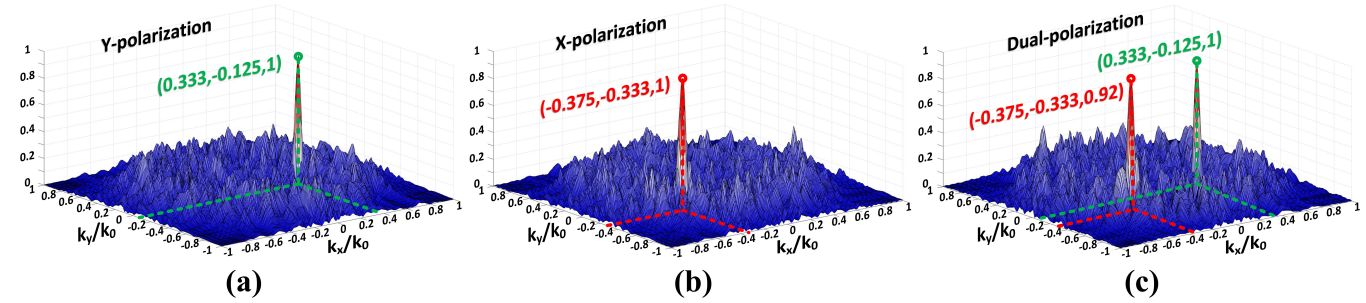

Fig. 6. Estimated DoA patterns using the (a) y-polarized, (b) x-polarized, and (c) dual-polarized measurement modes.

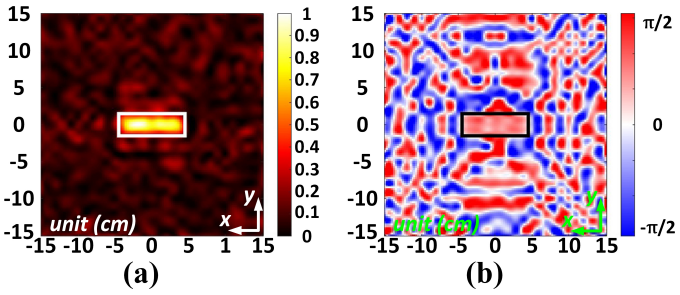

Fig. 7. CI results of the horizontal bar. (a) Amplitude of the reconstructed image using dual-polarized measurement modes; (b) Phase correlation between reconstructed images using the x- and y-polarized measurement modes.

IV. RMA-BASED ISAI SIMULATIONS

To verify the feasibility of the proposed RMA, full-wave ISAI simulations are conducted in CST Microwave Studio. The imaged scene is 30 cm × 30 cm in x- and y-directions, and it is discretized into 1681 (41 × 41) imaged pixels with a side length of 0.75 cm.

The RMA-based DoA estimation experiment is firstly carried out according to the configuration shown in Fig. 1(a). In this work, two far-field sources with orthogonal polarizations are employed, with respective incident angles of $(\theta, \varphi)^{y_{pol}}$ = (20°, -20°) and $(\theta, \varphi)^{x_{pol}}$ = (-30°, 40°). Following the procedure described in [15], the DoA patterns are reconstructed, as shown in Fig. 6. A peak-finding algorithm is then employed to determine k_x/k_0 and k_y/k_0 (collectively referred to as the *K-factor*), where $k_x/k_0 = \sin\theta\cos\varphi$ and $k_y/k_0 = \sin\theta\sin\varphi$ [32]. From Fig. 6, the K-factors of the two far-field sources are (0.333, -0.125) and (-0.375, -0.333), corresponding to incident angles of $(\theta, \varphi)^{y_{pol}}_{est}$ = (20.855°, -20.556°) and $(\theta, \varphi)^{x_{pol}}_{est}$ = (-30.115°, 41.634°), respectively. The close agreement between the estimated and true incident angles confirms the validity of the RMA-based DoA estimation method. Moreover, a comparison between Fig. 6(a) and 6(b) reveals that when only the y- or x-polarized measurement modes are employed, the incident angles can be determined solely for far-field sources matching the respective polarization. However, as shown in Fig. 6(c), when dual-polarized measurement modes are utilized, all far-field sources can be accurately estimated regardless of their polarizations.

Next, a horizontal metallic bar (3 cm × 9 cm), positioned 50 cm from the RMA, serves as the imaged target for the CI experiments (see Fig. 1(b)). The results are shown in Fig. 7. Fig. 7(a) presents the amplitude of the reconstructed image obtained using the dual-polarized measurement modes, clearly revealing the target. To highlight the geometric features of the target, the correlation between the reconstructed images from the x- and y-polarized measurement modes is calculated following the approach in [22]. This process allows extraction of the bar's orientation from the phase value, with values close to -π/2 and π/2 indicating vertical and horizontal orientations, respectively [27], as demonstrated in Fig. 7(b).

In summary, the results of both the DoA estimation and CI experiments collectively demonstrate the feasibility of RMA-based ISAI using a unified hardware platform.

V. CONCLUSION

In this paper, an RMA for ISAI applications was proposed. The RMA comprised a set of randomly distributed switchable meta-atoms with two orthogonal orientations to enable dual-polarized radiation. By manipulating the *on/off* states of the PIN diodes loaded onto the RMA, switchable meta-atoms are selectively deactivated or activated, thereby dynamically altering the aperture mask and generating low-correlated field patterns. A total of 100 such field patterns were selected as measurement modes to implement RMA-based ISAI (i.e., DoA estimation and CI). The incident angles of the far-field sources were accurately estimated, and both the image and orientation of the target were successfully retrieved, confirming the feasibility of the proposed RMA. This design offers an alternative technology for ISAI applications and is a promising unified hardware platform for IoT applications.

ACKNOWLEDGMENT

This work was funded by the Leverhulme Trust under Research Leadership Award under Grant RL-2019-019.

REFERENCES

[1] O. Yurduseven, T. Fromenteze, C. Decroze, and V. Fusco, "Frequency-diverse computational automotive radar technique for debris detection," *IEEE Sens. J.*, vol. 20, no. 22, pp. 13167-13177, Nov. 2020.

[2] X. Qiao, C. Jiang, P. Li, Y. Yuan, Q. Zeng, L. Bi, S. Song, J. Kim, D. D. Feng, and Q. Huang, "Improving breast tumor segmentation in PET via attentive transformation based normalization," *IEEE J. Biomed. Health*, vol. 26, no. 7, pp. 3261-3271, Jul. 2022.

[3] D. M. Sheen, D. L. Mcmakin, and T. E. Hall, "Three-dimensional millimeter-wave imaging for concealed weapon detection," *IEEE Trans. Microw. Theory Techn.*, vol. 49, no. 9, pp. 1581-1592, Sept. 2001.

[4] S. Wang, G. Mao, and J. A. Zhang, "Joint time-of-arrival estimation for coherent UWB ranging in multipath environment with multi-user interference," *IEEE Trans. Signal Process.*, vol. 67, no. 14, pp. 3743-3755, Jul. 2019.

[5] W. Li, N. Wang, and J. Qi, "Direct angle of arrival (AOA) estimation using a metasurface antenna with single frequency phaseless measurements obeyed schwarz inequality," *IEEE Trans. Microw. Theory Techn.*, vol. 72, no. 4, pp. 2677-2685, Apr. 2024.

[6] A. M. Molaei, B. Zakeri, S. M. H. Andargoli, M. A. B. Abbasi, V. Fusco, and O. Yurduseven, "A comprehensive review of direction-of-arrival estimation and localization approaches in mixed-field sources scenario," *IEEE Access*, vol. 12, pp. 65883-65918, May 2024.

[7] A. del Hoyo Vijande, Y. Álvarez-López, J. Laviada, and F. Las-Heras Andrés, "Compressive phaseless imaging based on synthetic aperture radar techniques," *IEEE Trans. Instrum. Meas.*, vol. 74, pp. 1-12, Apr. 2025, Art. no. 8004112.

[8] K. Han and S. Hong, "High-resolution phased-subarray MIMO radar with grating lobe cancellation technique," *IEEE Trans. Microw. Theory Techn.*, vol. 70, no. 5, pp. 2775-2785, May 2022.

[9] M. F. Imani, J. N. Gollub, O. Yurduseven, A. V. Diebold, M. Boyarsky, T. Fromenteze, L. Pulido-Mancera, T. Sleasman, and D. R. Smith, "Review of metasurface antennas for computational microwave imaging," *IEEE Trans. Antennas Propag.*, vol. 68, no. 3, pp. 1860-1875, Mar. 2020.

[10] J. Zhang, M. García-Fernández, G. Álvarez-Narciandi, R. Sharma, J. Zhang, P. del Hougne, M. A. B. Abbasi, and O. Yurduseven, "ClassiGAN: Joint image reconstruction and classification in computational microwave imaging," *Trans. Radar Syst.*, vol. 3, pp. 441-452, Feb. 2025.

[11] C. Saigré-Tardif, R. Faqiri, H. Zhao, L. Li, and P. del Hougne, 'Intelligent meta-imagers: From compressed to learned sensing," *Appli. Phys. Rev.*, vol. 9, no. 9, Mar. 2022. Art. no. 011314.

[12] T. Fromenteze, O. Yurduseven, F. Berland, C. Decroze, D. R. Smith, and A. G. Yarovoy, "A transverse spectrum deconvolution technique for MIMO short-range fourier imaging," *IEEE Trans. Geosci. Remote Sens.*, vol. 57, no. 9, pp. 6311-6324, Sept. 2019.

[13] O. Yurduseven, M. A. B. Abbasi, T. Fromenteze, and V. Fusco, "Frequency-diverse computational direction of arrival estimation technique," *Sci. Rep.*, vol. 9, Nov. 2019, Art. no. 16704.

[14] M. A. B. Abbasi, V. Fusco, O. Yurduseven, R. I. Ansari, and S. L. Cotton, "Lens-loaded cavity antenna with detector diode as a direction-of-arrival estimator," *IEEE Antennas Wirel. Propag. Lett.*, vol. 20, no. 11, pp. 2176-2180, Nov. 2021.

[15] M. Zhao, L. Wang, S. Zhu, X. Chen, and O. Yurduseven, "Microwave integrated sensing and imaging using reconfigurable metacavity," *IEEE Trans. Microw. Theory Techn.*, vol. 73, no. 8, pp. 5592-5606, Aug. 2025.

[16] T. V. Hoang, R. Kumar, T. Fromenteze, M. García-Fernández, G. Álvarez-Narciandi, V. Fusco, and O. Yurduseven, "Frequency selective computational through wall imaging using a dynamically reconfigurable metasurface aperture," *IEEE Open J. Antennas Propag.*, vol. 3, pp. 353-362, Mar. 2022.

[17] T. V. Hoang, F. Fromenteze, M. A. B. Abbasi, C. Decroze, M. Khalily, V. Fusco, and O. Yurduseven, "Spatial diversity improvement in frequency-diverse computational imaging with a multi-port antenna," *Results Phys.*, vol. 22, Mar. 2021, Art. no. 103906.

[18] K. Tekbıyık, O. Yurduseven, and G. K. Kurt, "Graph attention network-based single-pixel compressive direction of arrival estimation," *IEEE Commun. Lett.*, vol. 26, no. 3, pp. 562-566, Mar. 2022.

[19] T. V. Hoang, V. Fusco, M. A. B. Abbasi, and O. Yurduseven, "Single-pixel polarimetric direction of arrival estimation using programmable coding metasurface aperture," *Sci. Rep.*, vol. 11, Dec. 2021, Art. no. 23830.

[20] M. Zhao, S. Zhu, D. P. Lynch, Y. Nian, T. Fromenteze, M. Khalily, X. Chen, V. Fusco, and O. Yurduseven, "Frequency-diverse metacavity Cassegrain antenna for differential coincidence imaging," *IEEE Trans. Antennas Propag.*, vol. 71, no. 11, pp. 9054–9059, Nov. 2023.

[21] M. Zhao, S. Zhu, D. Li, T. Fromenteze, M. Khalily, X. Chen, V. Fusco, and O. Yurduseven, "Frequency-diverse bunching metasurface antenna for microwave computational imaging," *IEEE Trans. Antennas Propag.*, vol. 72, no. 5, pp. 3950-3961, May 2024.

[22] M. Zhao, S. Zhu, T. Fromenteze, M. A. B. Abbasi, X. Chen, Y. Huang, and O. Yurduseven, "Dual-polarized frequency-diverse metaimager for computational polarimetric imaging," *IEEE Trans. Antennas Propag.*, vol. 72, no. 7, pp. 5479-5488, Jul. 2024.

[23] J. Han, L. Li, S. Tian, G. Liu and Y. Shi, "Millimeter-wave imaging using 1-bit programmable metasurface: Simulation model, design, and experiment," *IEEE J. Em. Sel. Top. C.*, vol. 10, no. 1, pp.52-61, Mar. 2020.

[24] B. Liu, J. Wu, Q. Zhang, and H. Wong, "High-speed wide-angle sensing and imaging by wideband metasurfaces with joint frequency, polarization, and spatial diversities," *Laser Photonics Rev.*, Apr. 2024. Art. no. 2400207.

[25] Q. Zhang, J. Wang, H. Yu, J. Liu, J. Wang, C. Zhu, Y. Li, X. Li, Q. Xi, B. Zhang, Z. Zhu, and L. Ran, "Computational microwave imaging with a 1-bit phase reconfigurable transmitarray," *IEEE Trans. Microw. Theory Techn.*, vol. 72, no. 12, pp. 7004-7017, Dec. 2024.

[26] M. Khalily, O. Yurduseven, T. J. Cui, Y. Hao, and G. V. Eleftheriades, "Engineered electromagnetic metasurfaces in wireless communications: Applications, research frontiers and future directions," *IEEE Commun. Mag.*, vol. 60, no. 10, pp. 88-94, Oct. 2022.

[27] T. Fromenteze, O. Yurduseven, M. Boyarsky, J. Gollub, D. L. Marks, and D. R. Smith, "Computational polarimetric microwave imaging," *Opt. Express*, vol. 25, no. 22, pp. 27488-27505, Oct. 2017.

[28] M. Zhao, S. Zhu, X. Chen, T. Fromenteze, Q. H. Abbasi, A. Alomainy, V. Fusco, and O. Yurduseven, "Three-dimensional computational polarimetric imaging with a hyperuniform frequency-diverse metacavity transceiver," *IEEE Trans. Instrum. Meas.*, vol. 73, pp. 1-11, Mar. 2024, Art. no. 8002511.

[29] M. Zhao, S. Zhu, J. Zhang, X. Chen, and O. Yurduseven, "Compact metacavity antenna with enhanced radiation uniformity for narrowband microwave computational polarimetric imaging," *IEEE Trans. Antennas Propag.*, vol. 73, no. 8, pp. 6139-6144, Aug. 2025.

[30] T. V. Hoang, V. Fusco, T. Fromenteze, and O. Yurduseven, "Computational polarimetric imaging using two-dimensional dynamic metasurface apertures," *IEEE Open J. Antennas Propag.*, vol. 2, pp. 488-497, Mar. 2021.

[31] R. Peng, O. Yurduseven, T. Fromenteze, and D. R. Smith, "Advanced Processing of 3D Computational Microwave Polarimetry Using a Near-Field Frequency-Diverse Antenna," *IEEE Access*, vol. 8, pp. 166261-166272, Sept. 2020.

[32] M. Zhao, L. Wang, S. Zhu, M. A. B. Abbasi, T. Fromenteze, and O. Yurduseven, "Towards a reconfigurable metacavity antenna for computational imaging and DoA estimation," in *Proc. 18th Eur. Conf. Antennas Propag. (EuCAP)*, Mar. 2024, pp. 1–5.

[33] O. Yurduseven, D. L. Marks, T. Fromenteze, J. N. Gollub, and D. R. Smith, "Millimeter-wave spotlight imager using dynamic holographic metasurface antennas," *Opt. Express*, vol. 25, no. 15, pp. 18230-18249, Jul. 2017.

[34] M. Zhao, J. Zhang, A. Li, M. García-Fernández, G. Álvarez-Narciandi, S. Zhu, and O. Yurduseven,"Microwave computational imaging-based near-field measurement method," *IEEE Antennas Wirel. Propag. Lett.*, vol. 23, no. 11, pp. 3392-3396, Nov. 2024.

[35] M. Zhao, S. Zhu, R. Sharma, A. M. Molaei, X. Chen, and O. Yurduseven, "Metamaterial iris-based cavity antenna for mm-wave computational polarimetric imaging," *IEEE Antennas Wirel. Propag. Lett.*, vol. 23, no. 11, pp. 3367-3371, Nov. 2024.

[36] A. Li, M. Zhao, D. P. Lynch, S. Zhu, M. A. B. Abbasi, and O. Yurduseven, "Frequency-diverse reflection metasurface antenna design for computational microwave imaging," *IEEE Open J. Antennas Propag.*, vol. 5, no. 5, pp. 1240-1248, Oct. 2024.

[37] A. M. Molaei, T. Fromenteze, V. Skouroliakou, T. V. Hoang, R. Kumar, V. Fusco, and O. Yurduseven, "Development of fast fourier-compatible image reconstruction for 2D near-field bistatic microwave imaging with dynamic metasurface antennas," *IEEE Trans. Veh. Technol.*, vol. 71, no. 12, pp. 13077-13090, Dec. 2022.

[38] O. Yurduseven, M. F. Imani, H. Odabasi, J. Gollub, G. Lipworth, A. Rose, and D. R. Smith, "Resolution of the frequency diverse metamaterial aperture imager," *Prog. Electromagn. Res.*, vol. 150, pp. 97-107, 2015.

[39] M. Zhao, S. Zhu, H. Huang, D. Hu, X. Chen, J. Chen, and A. Zhang, "Frequency-diverse metamaterial cavity antenna for microwave coincidence imaging," *IEEE Antennas Wirel. Propag. Lett.*, vol. 20, no. 6, pp. 1103-1107, Jun. 2021.